ANNALS OF MATHEMATICAL SCIENCES AND APPLICATIONS
, , ,

Two-stage dimension reduction for noisy high-dimensional images and application to Cryogenic Electron Microscopy

SZU-CHI CHUNG, SHAO-HSUAN WANG, PO-YAO NIU, SU-YUN HUANG, WEI-HAU CHANG, I-PING TU*†

Principal component analysis (PCA) is arguably the most widely used dimension-reduction method for vector-type data. When applied to a sample of images, PCA requires vectorization of the image data, which in turn entails solving an eigenvalue problem for the sample covariance matrix. We propose herein a two-stage dimension reduction (2SDR) method for image reconstruction from high-dimensional noisy image data. The first stage treats the image as a matrix, which is a tensor of order 2, and uses multilinear principal component analysis (MPCA) for matrix rank reduction and image denoising. The second stage vectorizes the reduced-rank matrix and achieves further dimension and noise reduction. Simulation studies demonstrate excellent performance of 2SDR, for which we also develop an asymptotic theory that establishes consistency of its rank selection. Applications to cryo-EM (cryogenic electronic microscopy), which has revolutionized structural biology, organic and medical chemistry, cellular and molecular physiology in the past decade, are also provided and illustrated with benchmark cryo-EM datasets. Connections to other contemporaneous developments in image reconstruction and high-dimensional statistical inference are also discussed.

KEYWORDS AND PHRASES: Generalized Information Criterion, Image Denoising and Reconstruction, Random Matrix Theory, Rank Selection, Stein's Unbiased Estimate of Risk.

1 Introduction

As noted by Chen et al. [9], determining the 3D atomic structure of biomolecules is important for elucidating the physicochemical mechanisms underlying vital processes, and major breakthroughs in this direction led to Nobel Prizes in Chemistry

*Corresponding author

†The authors are grateful to the Editor-in-Chief, Tze Leung Lai, for comments which improved the contents and its presentation significantly.This work is supported by Academia Sinica:AS-GCS-108-08 and MOST:106-2118-M-001-001 -MY2.

awarded to Roger Kornberg in 2006, Venkatraman Ramakrishnan, Thomas Steitz and Ada Yonath in 2009, and Brian Kobilka and Robert Lefkowitz in 2012. While X-ray crystallography played an important role in the last two discoveries, most large proteins resisted attempts at crystallization. Cryogenic electron microscopy (cyro-EM), which does not need crystals and is therefore amenable to structural determination of proteins that are refractory to crystallization [14], has emerged as an alternative to X-ray crystallography for determining 3D structures of macromolecules in the past decade, culminating in the Nobel Prize in chemistry awarded to Jacques Dubochet, Joachim Frank and Richard Henderson in 2017.

Chen et al. [9, pp. 260-261] first describe the workflow of cryo-EM image analysis and then focus on 2D clustering step that identifies structurally homogeneous sets of images after these images have gone through the alignment and other image processing steps of the workflow. The size of a cryo-EM image is often larger than 100 pixels measured in each direction. Treating an image as a vector with dimension p, which is the pixel number that exceeds $100 \times 100 = 10^4$, clustering a large set of these high-dimensional vectors is a challenging task, particularly because of the low signal-to-noise ratio (SNR) in each cryo-EM image. Chen et al. [9] proposed to use a novel clustering method called γ-SUP, in which γ refers to γ-divergence and SUP refers to "self-updating process", to address these challenges. Section 1.1 gives an overview of γ-SUP, while Section 1.2 describes visualization of multidimensional data using t-distributed Stochastic Neighbor Embedding (t-SNE) plots [24]. Section 1.3 provides an overview of multilinear principal component analysis (MPCA) which we developed its statistical properties in [20] and which will be used in Section 2 to develop a new two-stage dimension reduction (2SDR) method for high-dimensional noisy images. The first stage of 2SDR uses MPCA of a random matrix $\mathrm{X} \in \mathbb{R}^{p \times q}$ to represent the image, together with consistent selection of the actual rank (p_0, q_0) of the matrix X as a second-order tensor; representing a high-dimensional image as a matrix has computational advantages over image vectorization. The second stage of 2SDR carries out PCA for the vectorized reduced-rank image to achieve further dimension reduction; Sections 1.4 and 1.5 give an overview of the literature on rank selection for MPCA and PCA. In Section 3, applications of 2SDR to cryo-EM images are illustrated with benchmark datasets including 70s Ribosome and 80s Ribosome. We show that 2SDR can improve 2D image clustering to curate the clean particles and 3D classification to separate various conformations. In particular, for a dataset containing 11,000 volumes of 5 conformations of 70s Ribosome structure, we demonstrate that the t-SNE plot of 2SDR shows clear separation of the 5 groups, which illustrates the promise of the method for cryo-EM image analysis. The 80s Ribosome dataset, which has huge sample size and large pixel numbers, exemplifies the computational capability of 2SDR. Section 4 gives further discussion and concluding remarks.

1.1 γ-SUP and 2D clustering of cryo-EM images

An important step in the workflow of cryo-EM image analysis is 2D clustering to identify structurally and orientationally homogeneous sets of particle images. Sorzano et al [33] proposed a k-means algorithm which, for a given number of clusters, iteratively bisects the data to achieve this via a kernel-based entropy measure to mitigate the impact of outliers. Yang et al. [41] subsequently noted the difficulty to find good initial values and prespecify a manageable number of clusters, and found the k-means approach to be unsatisfactory. This led Chen et al. [9] to develop an alternative 2D clustering method called γ-SUP, in which γ stands for "γ-divergence" and SUP is abbreviation for "self-updating process" (introduced by Shiu and Chen [32]) and to demonstrate its superior performance in 2D clustering of cryo-EM images. Their γ-SUP algorithm can be viewed as an iteratively reweighted procedure using kernel weights that are inversely proportional to the γ-divergence $D_\gamma(f||g)$ of the chosen working parametric model (with a density function g) from the empirical measure with a kernel density function f; $0<\gamma<1$ and the case $\gamma\to 0$ gives the Kullback-Leibler divergence [15]. Chen et al. [9] propose to choose the working model of q-Gaussian distribution [2] so that the chosen model g has the smallest γ-divergence from f. The q-Gaussian distribution over $\mathbb{R}^p$, with $q<1+2p^{-1}$, is a generalization of the Gaussian distribution (corresponding to $q\to 1$) and has a density function of the form

$$g_q(x;\mu,\sigma)=(\sqrt{2\pi\sigma})^{-p}c_{p,q}\exp_q\left(-\|x-\mu\|^2/(2\sigma^2)\right),\quad x\in\mathbb{R}^p,$$

where $\exp_q(u)$ is the $q-$exponential function $\exp_q(u)=\{1+(1-q)u\}_+^{\frac{1}{1-q}}$ and $x_+=\max(x,0)$. For $1<q<1+2p^{-1}$, it corresponds to the multivariate t-distribution with $\nu=2(q-1)^{-1}-p$ degrees of freedom, whereas it has compact support for $q<1$, which is assumed by Chen et al. [9] in applications to cryo-EM images and for which $c_{p,q}=(1-q)^{p/2}\Gamma(1+p/2+(1-q)^{-1})/\Gamma(1+(1-q)^{-1})$.

Instead of working with a mixture density that requires specification of the number of mixture component and therefore encounters the same difficulty as the k-means approach, Chen et al. [9] propose to fit each component j with $g_q(\cdot;\mu_j,\sigma)$ separately but with same σ. For given σ, the minimizer μ_j^* of $D(f\parallel g_q(\cdot;\mu_j,\sigma))$ is given by the solution of the equation $\mu_j=\int yw(y;\mu_j,\sigma)dF(y)/\int w(y;\mu_j,\sigma)dF(y)$, where F is the distribution function with density f. Hence replacing F by the empirical distribution $\widehat{F}$ of the sample $\{y_i,1\le i\le n\}$ leads to the recursion

$$\widehat{\mu}_j^{(\ell+1)}=\frac{\int yw(y;\mu_j^{(\ell)},\sigma)d\widehat{F}(y)}{\int w(y;\mu_j^{(\ell)},\sigma)d\widehat{F}(y)},\quad \ell=0,1,\cdots$$

Using the SUP algorithm of [32] to replace $\widehat{F}$ by the empirical distribution $\widehat{F}^{(j)}$ of $\{\mu_i^{(j)} : 1 \le i \le n\}$ leads to the γ-SUP recursion

$$\widehat{\mu}_j^{(\ell+1)} = \frac{\int y w(y;\mu_j^{(\ell)},\sigma) d\widehat{F}^{(\ell)}(y)}{\int w(y;\mu_j^{(\ell)},\sigma) d\widehat{F}^{(\ell)}(y)}, \quad \ell = 0,1,\cdots,$$

in which $w_{ij}^{(\ell)}$ has the explicit formula $w_{ij}^{(\ell)} = \exp_{1-s}\left(-\left\|(\widehat{\mu}_j^{(\ell)} - \widehat{\mu}_i^{(\ell)})/\tau\right\|^2\right)$, where $\tau = \sqrt{2}\sigma/\sqrt{\gamma-(1-q)} > 0$ and $s = (1-q)/\{\gamma-(1-q)\} > 0$. This explicit formula is derived by Chen et al. [9, p269] who also show that eventually " γ-SUP converges to certain K clusters, where K depends on the tuning parameters (τ, s) but otherwise is data-driven." Another advantage of γ-SUP is that σ is absorbed in the tuning parameter τ, hence selection of τ obviates the need to select σ. As pointed out by Chen et al. [9, p.268], γ-SUP "involves (s,τ) as the tuning parameters" and "numerical studies have found that γ-SUP is quite insensitive to the choice of s and that τ plays the decisive role in the performance of γ-SUP", for which they suggest to use a small positive value (e.g. 0.025) of s and a "phase transition plot" for practical implementation in their Section 4, where performance of a clustering method is measured by "purity" and "c-impurity" numbers that will be discussed below in Section 3.2.

1.2 t-distributed stochastic neighbor embedding (t-SNE)

Data visualization is the graphical representation of data, for which tools from multiple disciplines have been developed, including computer graphics, infographics, and statistical graphics. Recent advances, which include t-SNE and Laplacian eigenmap, focus on complex data belonging to a low-dimensional manifold embedded in a high-dimensional space. Laplacian eigenmap builds a graph from neighborhood information of the dataset. Using the adjacency matrix w_{ij} to incorporate this neighborhood information, Belkin and Niyogi [6] consider the optimization problem of choosing configuration points y_i to minimize $\sum_{j>i} w_{ij}||y_j - y_i||^2$, which forces y_i and y_j to be close to each othe if w_{ij} is large, and apply graph theory and the Laplace-Beltrami operator to formulate the optimization problem as an eigenvalue problem [11]. However, until Maaten and Hinton [24] developed t-SNE for data visualization in 2008, no visualization was able to separate the MNIST benchmark dataset, consisting of 28×28 pixel images each of which has a hand-written digit from 0 to 9, into ten groups (corresponding to the ten digits).

Similar to Laplacian eigenmap, t-SNE also has underpinnings in local information of the dataset $\{X_1,\ldots,X_n\}$, with distance measure $d(X_i,X_j)$ between X_i and

X_j. Instead of using the adjacency matrix of a graph to incorporate the local information, t-SNE uses a Gaussian Kernel to transform the distance matrix $d(X_i,X_j)$ first into a probability transition matrix $\widetilde{\pi}_{ij} \propto \exp(-d(X_i,X_j)/2\sigma_i^2)$, i.e., $\widetilde{\pi}_{ij}$ is the conditional probability of moving from position X_j given the initial position X_i, and then into a probability mass function $p_{ij} = (\pi_{ij}+\pi_{ji})/(2n)$ over pairs of configuration points y_i and y_j. This probability distribution enables Maaten and Hinton [24] to combine ideas from multidimensional scaling [26] which minimizes $\sum_{j>i}(d_{ij} - d_{ij}^*)^2$, where d_{ij} (respectively, d_{ij}^*) is the Euclidean distance between configuration points y_i and y_j in the dataset (respectively, in a low-dimensional subspace of the high-dimensional space), to choose the t-distribution for "stochastic neighbor embedding" (hence t-SNE) that minimizes the Kullback-Leibler divergence $I(p,q) = \sum_i \sum_j p_{ij} \log(p_{ij}/q_{ij})$, where $q_{ij} = (1+||y_i - y_j||^2)^{-1} / \sum_{k\neq l}(1+||y_k - y_l||^2)^{-1}$ for configuration points y_i and y_j with $i \neq j$, which corresponds to the density function of the t-distribution for $||y_i - y_j||$ with one degree of freedom. Applying stochastic gradient to minimize $I(p,q)$ yields

$$\frac{\delta I}{\delta y_i} = 4\sum_j (p_{ij} - q_{ij})(y_j - y_i)(1+||y_j - y_i||^2)^{-1},$$

which then leads to the iterative scheme

$$y_i^{(t)} = y_i^{(t-1)} + \eta(\frac{\delta I}{\delta y_i}) + \alpha^{(t)}(y_i^{(t-1)} - y_i^{(t-2)}),$$

where η is the "learning rate" and $\alpha^{(t)}$ is the "momentum" at iteration t of machine learning algorithms. How to choose them and σ_i^2 in p_{ij} (via $\widetilde{\pi}_{ij}$) is also discussed in [24].

1.3 PCA and MPCA

Let $X, X_1, \cdots, X_n$ be i.i.d. $p \times q$ random matrices. Let $y = \mathrm{vec}(X_i)$, where vec is the operator of matrix vectorization by stacking the matrix into a vector by columns. The statistical model for PCA is

$$y = \mu + \Gamma \nu + \varepsilon, \tag{1.1}$$

where μ is the mean, $\nu \in \mathbb{R}^r$ with $r \leq pq$, Γ is a $pq \times r$ matrix with orthonormal columns, and ε is independent of ν with $\mathrm{E}(\varepsilon) = 0$ and $\mathrm{Cov}(\varepsilon) = c\, I_{pq}$. The zero-mean vector ν has covariance matrix $\Delta = \mathrm{diag}(\delta_1, \delta_2, \cdots, \delta_r)$ with $\delta_1 \geq \delta_2 \geq \cdots \geq \delta_r > 0$. The estimate $\widehat{\Gamma}$ contains the first r eigenvectors of the sample covariance matrix $S_n = n^{-1}\sum_{i=1}^n (y_i - \overline{y})(y_i - \overline{y})^\top$, and $\mathrm{vec}(\overline{X}) + \widehat{\Gamma}\widehat{v}_i$ provides a reconstruction

of the noisy data $\text{vec}(X_i)$. The computational cost, which increases with both the sample size n and the dimension pq, becomes overwhelming for high-dimensional data. For example, the 80s Ribosome dataset in [40] has more than $n = 100,000$ images of dimension pq (after vectorization) with $p = q = 360$. The computational complexity of solving for the first r eigenvectors of S_n is $O((pq)^2 r) = O(10^{10} \times r)$ in this case, as shown by Pan and Chen [27], which may be excessive for many users. An alternative to matrix vectorization is MPCA [20, 42] or higher-order singular value decomposition (HOSVD) [13], and both methods have been found to reconstruct images from noisy data reasonably well while MPCA has better asymptotic performance than HOSVD [20], hence we only consider MPCA in the sequel.

MPCA models the $p \times q$ random matrix X as

$$X = Z + \mathscr{E} \in \mathbb{R}^{p\times q}, \quad Z = M + AUB^\top, \tag{1.2}$$

where $M \in \mathbb{R}^{p\times q}$ is the mean, $U \in \mathbb{R}^{p_0\times q_0}$ is a random matrix with $p_0 \le p$, $q_0 \le q$, A and B are non-random $p \times p_0, q \times q_0$ matrices with orthogonal column vectors, $\mathscr{E}$ is a zero-mean radnom vector independent of U such that $\text{Cov}(\text{vec}(\mathscr{E})) = \sigma^2 I_{pq}$. Ye [42] proposed to use generalized low-rank approximations of matrices to estimate A and B. Given (p_0, q_0), $\widehat{A}$ consists of the leading p_0 eigenvectors of the covariance matrix $\sum_{i=1}^n (X_i - \overline{X}) P_{\widehat{B}} (X_i - \overline{X})^\top$, and $\widehat{B}$ consists of the leading q_0 eigenvectors of $\sum_{i=1}^n (X_i - \overline{X})^\top P_{\widehat{A}} (X_i - \overline{X})$, where the matrix $P_{\widehat{A}} = \widehat{A}\widehat{A}^\top$ (respectively, $P_{\widehat{B}} = \widehat{B}\widehat{B}^\top$) is the projection operator into the span of the column vectors of $\widehat{A}$ (respectively, $\widehat{B}$). The estimates can be computed by an iterative procedure that usually takes no more than 10 iterations to converge. Replacing A and B by their estimates $\widehat{A}$ and $\widehat{B}$ in (1.2) yields

$$\widehat{U}_i = \widehat{A}^\top (X_i - \overline{X}) \widehat{B}, \text{ hence } \widehat{A}\widehat{U}_i\widehat{B}^\top = P_{\widehat{A}} (X_i - \overline{X}) P_{\widehat{B}}, \tag{1.3}$$

i.e., $\text{vec}(\widehat{A}\widehat{U}_i\widehat{B}^\top) = P_{\widehat{B}\otimes\widehat{A}} \text{vec}(X_i - \overline{X})$ where $\otimes$ denotes the Kronecker product and $P_{\widehat{B}\otimes\widehat{A}} = (\widehat{B}\widehat{B}^\top) \otimes (\widehat{A}\widehat{A}^\top)$.

Hung et al. [20, p.571] used the notion of the Kronecker envelope introduced by Li et al. [23] to connect MPCA and PCA models. For the PCA model (1.1) with $y = \text{vec}(X)$, they note form Theorem 1 of [23] that there exists a full rank $p_0 q_0 \times r$ matrix G such that $\Gamma = (B \otimes A)G$ for which (1.1) becomes

$$\text{vec}(X) = \text{vec}(M) + (B \otimes A) G\nu + \text{vec}(\mathscr{E}) \in \mathbb{R}^{pq}, \text{ with } \nu \in \mathbb{R}^r. \tag{1.4}$$

The components of ν in (1.4) are pairwise uncorrelated, whereas those of $\text{vec}(U)$ in the MPCA model (1.2) are not; the subspace $\text{span}(B \otimes A)$ is "the unique minimal

subspace that contains span(Γ)" and is "called the Kronecker envelope of Γ". From (1.3) and (1.4), we need to specify (p_0, q_0) and r, respectively, and the following two subsections will summarize previous works on how to select them.

1.4 Rank selection for MPCA

We first review the recent work of Tu et al. [36] using Stein's unbiased risk estimate (SURE) to derive a rank selection method for the MPCA model, under the assumption that $\text{vec}(\mathscr{E})$ has a multivariate normal distribution with mean 0 and covariance matrix $\sigma^2 I_{pq}$. They note that "with the advent of massive data, often endowed with tensor structures," such as in images and videos, gene-gene environment interactions, dimension reduction for tensor data has become an important but challenging problem. In particular, Tao et al. [35] introduced a mode-decoupled probabilistic model for tensor data, assuming independent Gaussian random variables for the stochastic component of the tensor, and applied the information criteria in AIC and BIC independently to each projected tensor mode. In the special case of the MPCA model for tensors of order 2, the stochastic components correspond to the entries of U in (1.2), which are pairwise correlated and therefore not independent. For the MPCA model (1.2), Tu et al. [36] introduce the risk function

$$
\begin{aligned}
(1.5) \qquad R(p_0, q_0; \sigma^2) &= \sum_{k=1}^{n} \mathrm{E}\|Z_k - \widehat{Z}_k\|_F^2 \\
&= \sum_{k=1}^{n} \left[\mathrm{E}\|X_k - \widehat{Z}_k\|_F^2 - 2\mathrm{E}[\mathrm{tr}\{\mathscr{E}_k^\top (X_k - \widehat{Z}_k)\}] + \mathrm{E}\|\mathscr{E}_k\|_F^2 \right]
\end{aligned}
$$

to be used as the risk that SURE estimates by using Stein's identity [34, 37] under the assumption that $\text{vec}(\mathscr{E}) \sim N(0, \sigma^2 I_{pq})$. The last (i.e., third) summand in (1.5) is $npq\sigma^2$, the first summand can be estimated by $\sum_{k=1}^{n} |X_k - \widehat{A}\widehat{U}_k\widehat{B}^\top\|_F^2$, and the second summand is equal to

$$
(1.6) \qquad -2\sigma^2 \sum_{k=1}^{n} \mathrm{E}\left[\mathrm{tr}\left\{ \frac{\partial \text{vec}(X_k - \widehat{Z}_k)}{\partial \text{vec}(X_k)^\top} \right\} \right] = -2npq\sigma^2 + 2\sigma^2 \sum_{k=1}^{n} \mathrm{E}\left[\mathrm{tr}\left\{ \frac{\partial \text{vec}(\widehat{Z}_k)}{\partial \text{vec}(X_k)^\top} \right\} \right],
$$

by Stein's identity. Letting Σ denote the covariance matrix of $\text{vec}(X)$ in (1.2) and $\widehat{\Sigma} = n^{-1}\sum_{i=1}^{n} \text{vec}(X_i - \bar{X})\text{vec}(X_i - \bar{X})^\top$ be its estimate, Tu et al. [36, pp. 35-37] note that $\text{vec}(\widehat{Z}_k) = P_{\widehat{B}\otimes\widehat{A}}\text{vec}(X_k)$ and that $\widehat{A}$ and $\widehat{B}$ depend on $\widehat{\Sigma}$, and use the chain rule to compute the derivative $(\frac{\partial}{\partial \text{vec}(X_k)^\top})(P_{\widehat{B}\otimes\widehat{A}}\text{vec}(X_k)) = (\frac{\partial (P_{\widehat{B}\otimes\widehat{A}}\text{vec}(X_k))}{\partial (\text{vec}(\widehat{\Sigma}))^\top})(\frac{\partial \text{vec}(\widehat{\Sigma})}{\partial \text{vec}(X_k)^\top})$ and then prove that the second summand of (1.6) can be estimated by $2\sigma^2 \text{df}_{(p_0,q_0)}$,

where

$$\mathrm{df}_{(p_0,q_0)} = pq + (n-1)p_0q_0 + \sum_{i=1}^{p_0}\sum_{\ell=p_0+1}^{p}\frac{\widehat{\lambda}_i+\widehat{\lambda}_\ell}{\widehat{\lambda}_i-\widehat{\lambda}_\ell} + \sum_{j=1}^{q_0}\sum_{\ell=q_0+1}^{q}\frac{\widehat{\xi}_j+\widehat{\xi}_\ell}{\widehat{\xi}_j-\widehat{\xi}_\ell} \tag{1.7}$$

is the "degree of freedom" and the $\widehat{\lambda}_i$ (respectively, $\widehat{\xi}_j$) are the eigenvalues, in decreasing order of their magnitudes, of $n^{-1}\sum_{k=1}^{n}(X_k-\overline{X})P_{\widehat{B}}(X_k-\overline{X})^\top$ (respectively, $n^{-1}\sum_{k=1}^{n}(X_k-\overline{X})P_{\widehat{A}}(X_k-\overline{X})^\top$). Their Section 3.2 gives interpretations and discussion of $\mathrm{df}_{(p_0,q_0)}$, and their proof of (1.7) keeps the numerator terms to be column vectors and denominator terms to be row vectors, and uses the identity $\mathrm{vec}(ABC) = (C^\top \otimes A)\mathrm{vec}(B)$ together with

$$\begin{aligned}\sum_{i=1}^{n} X_i\widehat{B}\widehat{B}^\top X_i^\top &= \sum_{i=1}^{n} X_i\left(\sum_{j=1}^{q_0}\widehat{b}_j\widehat{b}_j^\top\right)X_i^\top = \sum_{i=1}^{n}\sum_{j=1}^{q_0}(X_i\widehat{b}_j)(X_i\widehat{b}_j)^\top \\ &= \sum_{i=1}^{n}\sum_{j=1}^{q_0}\Big((b_j^\top\otimes I_p)\mathrm{vec}(X_i)\Big)\Big(\mathrm{vec}(X_i)^\top(b_j\otimes I_p)\Big) \\ &= n\sum_{j=1}^{q_0}\Big\{(b_j^\top\otimes I_p)\widehat{\Sigma}(b_j\otimes I_p)\Big\}\end{aligned}$$

in which $\widehat{B} = \{\widehat{b}_1,\ldots,\widehat{b}_{q_0}\}$, where $\widehat{b}_j$ is the normalized eigenvector of $n^{-1}\sum_{i=1}^{n}X_i^\top\widehat{A}\widehat{A}^\top X_i$ associated with the eigenvalue $\widehat{\xi}_j$, and we have assumed $\overline{X}=0$ to simplify the notation involving $X_i-\overline{X}$.

The rank selection method chooses the rank pair $(\widehat{p}_0,\widehat{q}_0)$ to minimize over (p_0,q_0) the criterion

$$\mathrm{SURE}(p_0,q_0;\sigma^2) = n^{-1}\sum_{k=1}^{n}\|X_k-\widehat{A}\widehat{U}_k\widehat{B}^\top\|_F^2 + 2n^{-1}\sigma^2\mathrm{df}_{(p_0,q_0)} - pq\sigma^2, \tag{1.8}$$

in which σ^2 is assumed known or replaced by its estimate $\widehat{\sigma}^2$ descirbed in Section 3.3 and Algorithms 1 and 2 of Tu et al. [36]. A basic insight underlying high-dimensional covariance matrix estimation is that the commonly used average of tail eigenvalues tends to under-estimate σ^2 because the empirical distribution (based on a sample of size n) of the eigenvalues of I_p converges weakly to the Marchenko-Pastur distribution as $n\to\infty$ and p/n converges to a positive constant. For a large random martix, Ulfarsson and Solo [37] use an upper bound on the number of eigenvalues for its bulk and Tu et al. [36] modify this idea in their Algorithm 2 for the PCA model, which they then apply to the estimation of σ^2 in the MPCA model.

1.5 Rank selection for PCA

Noting that the commonly used information criterion AIC or BIC for variable selection in regression and time series models can be viewed as an estimator of the Kullback-Leibler divergence between the true model and a fitted model under the assumption that estimation is carried out by maximum likelihood for a parametric family that includes the true model, Konishi and Kitagawa [22] introduced a generalized information criterion (GIC) to relax the assumption in various ways. Recently Hung et al. [19] developed GIC for high-dimensional PCA rank selection, which we summarize below and will use in Section 2. A *generalized spiked covariance model* for an m-dimensional random vector has the spectral decomposition $\Sigma = \Gamma\Delta\Gamma^\top$ for its covariance matrix Σ, where $\Delta = diag(\delta_1, \ldots, \delta_m)$ with $\delta_1 > \cdots > \delta_r \gg \delta_{r+1} > \cdots > \delta_m$. We call r the "generalized rank". The sample covariance matrix S_n has the spectral decomposition $S_n = \Sigma_{j=1}^m \widehat{\delta}_j \widehat{\gamma}_j \widehat{\gamma}_j^\top$. Bai et al. [5] consider the special case of with $\delta_{r+1} = \cdots = \delta_m$, called the "simple spiked covariance model" and denoted by Σ_r. Under the assumption of i.i.d. Gaussian y_i, Bai et al. [5] prove consistency of AIC and BIC by using random matrix theory.

Following Konishi and Kitagawa's framework of model selection [22], Hung et al. [19] develop GIC for PCA rank selection in possibly misspecified generalized spiked covariance models with generalized rank r, for which they use b_r^{GIC} to denote the asymptotic bias correction, a major ingredient of GIC. Their Theorem 2 shows that under the distributional working model assumption of i.i.d. normal y_i with covariance matrix Σ_r, b_r^{GIC} can be expressed as

$$b_r^{\mathrm{GIC}} = \binom{r}{2} + \sum_{j=1}^{r}\sum_{\ell=r+1}^{m} \frac{\delta_\ell(\delta_j - \delta_r)}{\delta_r(\delta_j - \delta_\ell)} + r + \frac{(m-r)^{-1}\sum_{j=r+1}^m \delta_j^2}{\left\{(m-r)^{-1}\sum_{j=r+1}^m \delta_j\right\}^2}, \tag{1.9}$$

and the GIC-based rank selection criterion is

$$\widehat{r}_{\mathrm{GIC}} = \underset{r\le m}{\operatorname{argmin}} \left(\log|\widehat{\Sigma}_r| + \frac{\log n}{n}\widehat{b}_r^{\mathrm{GIC}} \right), \text{ where } \widehat{b}_r^{\mathrm{GIC}} \text{ replaces } \delta_i \text{ by } \widehat{\delta}_i \text{ in (1.9).}^{1} \tag{1.10}$$

Note that the last summand in (1.9) is ≥ 1, with equality if and only if $\delta_{r+1} = \cdots = \delta_m$, which is the simple spiked covariance model considered by Bai et al. [5],[2] and that GIC assumes y_i to be a random sample generated from an actual distribution with density function f and uses the Kullback-Leibler (KL) divergence

[1] The second summand on the right-hand side of (1.9) is actually a slight modification of that in [19] to achieve improved performance.

[2] Bai et al. [5] assume that the smallest $m-r$ eigenvalues of the true covariance matrix to be all equal in their proof of rank selection consistency of AIC or BIC.

$I(f,g)$ of a "working model" g that is chosen to have the smallest KL divergence from a family of densities; see [22, pp. 876-879]. Since f is unknown, Konishi and Kitagawa's idea is to estimate $I(f,g)$ via an "empirical influence function". Hung et al. [19] basically implement this approach in the context of PCA rank selection, for which random matrix theory and the Marchenko-Pastur distribution provide key tools in the setting of high-dimensional covariance matrices. However, even with these powerful tools, the estimate of $I(f,g)$ involves either higher moments of y_i "which can be unstable in practice" or the Stieltjes transform of the limiting Marchenko-Pastur distribution that is difficult to invert to produce explicit formulas for the bias-corrected estimate of $I(f,g)$. Hung et al. [19] preface their Theorem 2 with the comment that "a neat expression of b_r^{GIC} that avoids calculating high-order moments (of the y_i) can be derived under the working assumption of (their) Gaussianity" and follow up with Remark 2 and Sections 3.2 and 3.3 to show that this Gaussian assumption "is merely used to get an explicit neat expression for b_r^{GIC}" and "is not critical in applying" the rank selection criterion $\widehat{r}_{\mathrm{GIC}}$, which is shown in their Theorems 7,8 and 10 to be consistent under conditions that do not require Gaussianity.

2 Two-stage dimensional reduction (2SDR) for high-dimensional noisy images

We have reviewed in Sections 1.2–1.4 previous works on PCA and MPCA models, in particular the use of the "Kronecker envelope" $\mathrm{span}(B\otimes A)$ in (1.4) as an attempt to connect both models. This attempt, however, is incomplete because it does not provide an explicit algorithm to compute the "full rank $p_0q_0\times r$ matrix G" that is shown to "exist". In this section we define a new model , called *hybrid PCA* and denoted by $\mathrm{H_M PCA}$, in which the subscript M stands for MPCA and H stands for "hybrid" of MPCA and PCA. Specifically, $\mathrm{H_M PCA}$ assumes the MPCA model (1.2) with reduced rank (p_0,q_0) via the $p_0\times q_0$ random matrix U and then assumes a rank-r model, with $r\le p_0q_0$, for $\mathrm{vec}(U)$ to which a zero-mean random error ε with $\mathrm{Cov}(\varepsilon)=cI_{p_0,q_0}$ is added, as in (1.1). This leads to dimension reduction of $\mathrm{vec}(X-M-\mathscr{E})=\mathrm{vec}(A_{p_0}UB_{q_0}^\top)$ from p_0q_0 to r. Since $U=A_{p_0}^\top(X-M)B_{p_0}$ in view of (1.3), $\mathrm{vec}(A_{p_0}UB_{q_0}^\top)=P_{B_{q_0}\otimes A_{p_0}}\mathrm{vec}(X-M-\mathscr{E})$ is the projection of $X-M-\mathscr{E}$ into $\mathrm{span}(B_{q_0}\otimes A_{p_0})$, which has dimension r after this further rank reduction. The actual ranks, which we denote by (p_0^*,q_0^*) and r^*, are unknown as are the other parameters of the $\mathrm{H_M PCA}$ model, and 2SDR uses a sample of size n to fit the model and estimate the ranks.

The first stage of 2SDR uses (1.2) to model a noisy image X as a matrix. Ye's estimates $\widehat{A}$ and $\widehat{B}$ that we have described in the second paragraph of Section 1.2 depend on the given value of (p_0,q_0), which is specified in the criterion

SURE$(p_0,q_0;\sigma^2)$. Direct use of the criterion to search for (p_0,q_0) would therefore involve computation-intensive loops. To circumvent this difficulty, we make use of the analysis of the optimization problem associated with Ye's estimates at the population level by Hung et al. [20] and Tu et al. [36, pp. 27-28], who have shown that if the dimensionality is over-specified (respectively, under-specified) for span(A) (or span(B)), then it contains (respectively, is a proper subspace of) the true subspace. We therefore choose a rank pair (p_u,q_u) such that $p_u \geq p_0^*$ and $q_u \geq q_0^*$, where (p_0^*,q_0^*) is the true value of (p_0,q_0), and then solve for $(\widehat{A}_u,\widehat{B}_u)$ such that $\widehat{A}_u$ (respectively, $\widehat{B}_u$) consists of the leading p_u eigenvectors of $\sum_{k=1}^n (X_k-\overline{X})P_{\widehat{B}_u}(X_k-\overline{X})^\top$ (respectively, q_u eigenvectors of $\sum_{k=1}^n (X_k-\overline{X})P_{\widehat{A}_u}(X_k-\overline{X})^\top$); see Ye's estimate in the second paragraph of Section 1.2. This is tantamout to replacing (p_0^*,q_0^*) by the larger surrogates $(\widehat{p}_u,\widehat{q}_u)$ in $\mathrm{df}_{(p_0^*,q_0^*)}$ defined by (1.7). For given (p_0,q_0) with $p_0 \leq p_u$ and $q_0 \leq q_u$, let $\widehat{A}_{p_0}$ (respectively, $\widehat{B}_{q_0}$) be the submatrix consisting of the first p_0 (respectively, q_0) column vectors of $\widehat{A}_u$ (respectively, $\widehat{B}_u$). The rank selection criterion (1.8) into the SURE criterion is

(2.1)
$$\mathrm{S}_u^{(n)}(p_0,q_0;\sigma^2) = n^{-1}\sum_{k=1}^n \|X_k-\widehat{A}_{p_0}\widehat{U}_k\widehat{B}_{q_0}^\top\|_F^2 + 2n^{-1}\sigma^2\mathrm{df}_{p_0,q_0}^{(n)} - pq\sigma^2, \text{ where}$$

$$\mathrm{df}_{p_0,q_0}^{(n)} = pq+(n-1)p_0q_0+\sum_{i=1}^{p_0}\sum_{\ell=p_0+1}^{p}\frac{\widehat{\lambda}_i+\widehat{\lambda}_\ell}{\widehat{\lambda}_i-\widehat{\lambda}_\ell}+\sum_{j=1}^{q_0}\sum_{\ell=q_0+1}^{q}\frac{\widehat{\xi}_j+\widehat{\xi}_\ell}{\widehat{\xi}_j-\widehat{\xi}_\ell}, \tag{2.2}$$

in which $\widehat{U}_k = \widehat{A}_{p_0}^\top(X_k-\overline{X})\widehat{B}_{q_0}$ and

$$(\widehat{p}_0,\widehat{q}_0) = \mathrm{argmin}_{p_0\leq p_u,q_0\leq q_u}\mathrm{S}_u^{(n)}(p_0,q_0;\sigma^2). \tag{2.3}$$

In Section 2.1, we prove the consistency of $(\widehat{p}_0,\widehat{q}_0)$ as an estimate of (p_0^*,q_0^*).

After rank reduction via consistent estimation of (p_0^*,q_0^*) by $(\widehat{p}_0,\widehat{q}_0)$, the second stage of 2SDR achieves further rank reduction by applying the GIC-based rank selection criterion (1.10) to $S_{\mathrm{vec}(\widehat{U})} = n^{-1}\sum_{i=1}^n \mathrm{vec}(\widehat{U}_i)\mathrm{vec}(\widehat{U}_i)^\top$, where $\widehat{U}_i = \widehat{A}_{\widehat{p}_0}^\top(X_i-\overline{X})\widehat{B}_{\widehat{q}_0}$. Consider the corresponding matrix $\Sigma_{\mathrm{vec}(U)}$ at the population level and its ordered eigenvalues $\kappa_1 \geq \kappa_2 \geq \ldots$ and the orthonormal eigenvectors g_j associated with κ_j. Suppose $\mathrm{vec}(U-\varepsilon)$ belongs to an r-dimensional subspace. Since ε is independent of $\mathrm{vec}(U-\varepsilon)$ and has mean 0 and covariance matrix $cI_{p_0^*q_0^*}$, it then follows that

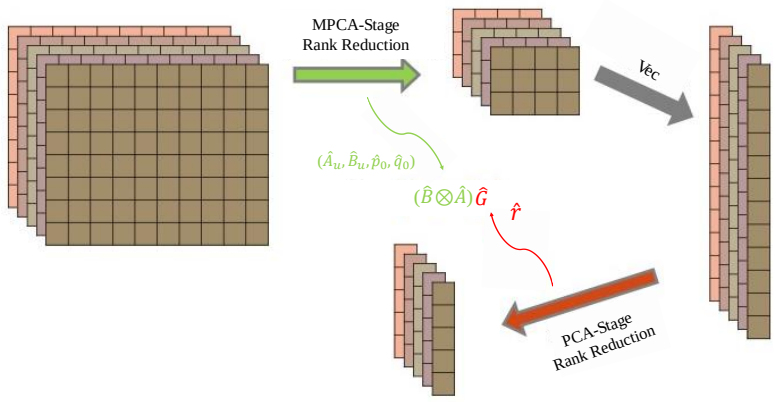

Figure 1: Schematic of 2SDR procedure.

$$\Sigma_{\mathrm{vec}(U)} = \sum_{j=1}^{r} \kappa_j g_j g_j^\top + c \sum_{j=r+1}^{p_0^* q_0^*} g_j g_j^\top, \tag{2.4}$$

Since $X_i = M + A_{p_0*} U_i B_{q_0*}^\top + \mathscr{E}_i$ with $\mathrm{Cov}(\mathscr{E}_i) = \sigma^2 I_{pq}$ in view of (1.2), it then follows that the covariance matrix of $\mathrm{vec}(X_i), 1 \le i \le n$, has eigenvalues

$$\kappa_1 + \sigma^2, \ldots, \kappa_r + \sigma^2, \underbrace{c + \sigma^2, \cdots c + \sigma^2}_{p_0^* q_0^* - r \text{ times}}, \underbrace{\sigma^2, \cdots, \sigma^2}_{pq - p_0^* q_0^* \text{ times}}. \tag{2.5}$$

Although $p_0^*, q_0^*, r, \sigma^2, c$ and other parameters such as $\kappa_1, \cdots, \kappa_r$ are actually unknown in (2.4) and (2.5), 2SDR uses a sample of size n to fit the model and thereby obtain the estimate of $\kappa_1, \cdots, \kappa_r$, which can be put into $\log|\widehat{\Sigma}_r|$ after replacing $p_0^* q_0^*$ by $\widehat{p}_0 \widehat{q}_0$; details are given in Section 2.1 and illustrated in Section 2.2.

2.1 Implementation and theory of 2SDR

The first paragraph of this section has already given details to implement the MPCA stage of 2SDR that yields $\widehat{A}_u, \widehat{B}_u, \widehat{A}_{p_0}, \widehat{B}_{q_0}, p_u, q_u, \widehat{p}_0$ and $\widehat{q}_0$, hence this subsection will provide details for the implementation of the basic idea underlying the second (PCA) stage of 2SDR described in the preceding paragraph and develop an asymptotic theory of 2SDR, particularly the consistency of the rank estimates in the $\mathrm{H_m PCA}$ model. Figure 1 is a schematic diagram of the 2SDR procedure, which

consists of 4 steps, the first two of which constitute the MPCA stage while the last two form the second (PCA) stage of 2SDR, based on a sample of $p \times q$ matrices X_i $(i = 1, \cdots, n)$ representing high-dimensional noisy images.

- **Step 1.** Fit the MPCA model (1.2) to the sample of size n to obtain the eigenvalues $\widehat{\lambda}_1, \cdots, \widehat{\lambda}_p$, $\widehat{\xi}_1, \cdots, \widehat{\xi}_q$ in (2.2) and the matrices $\widehat{A}_u$ and $\widehat{B}_u$.
- **Step 2.** Estimate σ^2 by the method of Tu et al. [36][3] described in the last paragraph of Section 1.3 and use the SURE rank selection criterion (2.3) to choose the reduced rank $(\widehat{p}_0, \widehat{q}_0)$.
- **Step 3.** Perform PCA on $S_{\mathrm{vec}(\widehat{U})} = n^{-1} \sum_{i=1}^n \mathrm{vec}(\widehat{U}_i)\mathrm{vec}(\widehat{U}_i)^\top$ to obtain its ordered eigenvalues $\widehat{\kappa}_1 \geq \cdots \widehat{\kappa}_{\widehat{p}_0 \widehat{q}_0}$.
- **Step 4.** For $r \leq \widehat{p}_0 \widehat{q}_0$, define (2.4) with κ_j replaced by $\widehat{\kappa}_j$, and compute $\log |\widehat{\Sigma}_r|$ and $\widehat{b}_r^{\mathrm{GIC}}$. Estimate the actual rank r^* by $\widehat{r}_{\mathrm{GIC}}$ defined in (1.10).

Hung et al. [20, Corollary 1] have shown that $\mathrm{vec}(P_{\widehat{B} \otimes \widehat{A}})$ is a $\sqrt{n}$-consistent estimate of $\mathrm{vec}(P_{B \otimes A})$ under certain regularity conditions, which we use to prove the following theorem on the consistency of $(\widehat{p}_0, \widehat{q}_0)$. The theorem needs the condition $c > \sigma^2$ because $2n^{-1}\sigma^2 \mathrm{df}_{p_0,q_0}^{(n)}$ in (2.1) can dominate the value of the criterion $\mathrm{S}_u^{(n)}(p_0, q_0; \sigma^2)$, especially when $p_0 < p_0^*$ and $q_0 < q_0^*$. The condition $c > \sigma^2$, or equivalently $c + \sigma^2 > 2\sigma^2$, ensures sufficiently large $\mathrm{S}_u^{(n)}(p_0, q_0; \sigma^2)$ to avoid erroneous rank selection in this case. The asymptotic analysis, as $n \to \infty$, in the following proof also shows how the condition $c > \sigma^2$ is used.

Theorem. *Assume that the MPCA model (1.2) holds and $c > \sigma^2$. Suppose $p_0^* \leq p_u$ and $q_0^* \leq q_u$. Then $\mathrm{P}(\widehat{p}_0 = p_0^* \text{ and } \widehat{q}_0 = q_0^*) \to 1$ as $n \to \infty$.*

Proof. The basic idea underlying the proof is the decomposition for the rank pair (p_0, q_0) with $p_0 \leq p_u$ and $q_0 \leq q_u$:

$$\mathrm{S}_u^{(n)}(p_0, q_0; \sigma^2) - \mathrm{S}_u^{(n)}(p_0^*, q_0^*; \sigma^2) = A_{1n} + A_{2n} + A_{3n} \tag{2.6}$$

consisting of three summands which can be analyzed separately by using different arguments to show that (2.6) is (a) at least of the order $n^{-1/2}$ in probability, (b) equal to $1 + o_P(1)$ if $p_0 < p_0^*$ or $q_0 < q_0^*$, and (c) of the $O_P(n^{-1/2}\tau_n)$ order if $p_0 \geq p_0^*$ and $q_0 \geq q_0^*$, ensuring that (2.6) is sufficiently above zero if $p_0 \neq p_0^*$ or $q_0 \neq q_0^*$. In view of (2.1), the left-hand side of (2.6) is equal to

$$\frac{1}{n} \sum_{i=1}^n \left\{ \|X_i - \widehat{A}_{p_0} \widehat{U}_i \widehat{B}_{q_0}\|_F^2 - \|X_i - \widehat{A}_{p_0^*} \widehat{U}_i \widehat{B}_{q_0^*}\|_F^2 \right\} + A_{3n}, \; A_{3n} = \frac{2\sigma^2}{n} (\mathrm{df}_{p_0 q_0}^{(n)} - \mathrm{df}_{p_0^* q_0^*}^{(n)}). \tag{2.7}$$

[3] We use 7/8 from the tail to estimate the variance of noise for the SURE method.

We next show that the first summand in (2.7) is equal to $A_{1n}+A_{2n}$, where

$$\begin{aligned} A_{1n} &= \frac{1}{n}\sum_{i=1}^{n}\|(P_{\widehat{B}_{q_0^*}}\otimes P_{\widehat{A}_{p_0^*}}-P_{\widehat{B}_{q_0}}\otimes P_{\widehat{A}_{p_0}})\mathrm{vec}(X_i)\|_F^2 \\ A_{2n} &= \frac{2}{n}\sum_{i=1}^{n}\langle(I_{pq}-P_{\widehat{B}_{q_0^*}}\otimes P_{\widehat{A}_{p_0^*}})\mathrm{vec}(X_i),\ (P_{\widehat{B}_{q_0^*}}\otimes P_{\widehat{A}_{p_0^*}}-P_{\widehat{B}_{q_0}}\otimes P_{\widehat{A}_{p_0}})\mathrm{vec}(X_i)\rangle, \end{aligned}$$

by writing $n^{-1}\sum_{i=1}^{n}\|X_i-\widehat{A}_{p_0}\widehat{U}_i\widehat{B}_{q_0}^{\top}\|_F^2$ as

$$\begin{aligned} &\frac{1}{n}\sum_{i=1}^{n}\|X_i-P_{\widehat{A}_{p_0^*}}X_iP_{\widehat{B}_{q_0^*}}+(P_{\widehat{A}_{p_0^*}}X_iP_{\widehat{B}_{q_0^*}}-P_{\widehat{A}_{p_0}}X_iP_{\widehat{B}_{q_0}})\|_F^2 \\ &=\frac{1}{n}\sum_{i=1}^{n}\|(I_{pq}-P_{\widehat{B}_{q_0^*}}\otimes P_{\widehat{A}_{p_0^*}})\mathrm{vec}(X_i)+(P_{\widehat{B}_{q_0^*}}\otimes P_{\widehat{A}_{p_0^*}}-P_{\widehat{B}_{q_0}}\otimes P_{\widehat{A}_{p_0}})\mathrm{vec}(X_i)\|_F^2 \\ &=\frac{1}{n}\sum_{i=1}^{n}\|X_i-\widehat{A}_{p_0^*}\widehat{U}_i\widehat{B}_{q_0^*}^{\top}\|_F^2+A_{1n}+A_{2n}. \end{aligned}$$

Let Σ be the covariance matrix of $\mathrm{vec}(X)$, $\widehat{\Sigma}=n^{-1}\sum_{i=1}^{n}\mathrm{vec}(X_i)\mathrm{vec}(X_i)^{\top}$, and note that $\widehat{\Sigma}=\Sigma+O_P(n^{-1/2})$. By Corollary 1 of [20],

(2.8)
$$\begin{aligned} &\widehat{A}_{p_0^*}=A_{p_0^*}+O_P(n^{-1/2}),\ \widehat{B}_{q_0^*}=B_{q_0^*}+O_P(n^{-1/2}), \\ &\widehat{A}_{p_0}=A_{p_0}+O_P(n^{-1/2}),\ \widehat{B}_{q_0}=B_{q_0}+O_P(n^{-1/2}),\ \text{for } 1\le p_0\le p_u \text{ and } 1\le q_0\le q_u. \end{aligned}$$

Note also that $A_{2n}=2\mathrm{tr}([P_{\widehat{B}_{(q_0^*\wedge q_0)}}\otimes P_{\widehat{A}_{(p_0^*\wedge p_0)}}-P_{\widehat{B}_{q_0}}\otimes P_{\widehat{A}_{p_0}}]\widehat{\Sigma})$. From this and (2.8), it follows that

$$A_{2n}=2\sigma^2\{(p_0^*\wedge p_0)(q_0^*\wedge q_0)-p_0q_0\}+O_P(n^{-1/2}). \tag{2.9}$$

Similar calculations show that $A_{1n}=\mathrm{tr}((P_{\widehat{B}_{q_0^*}}\otimes P_{\widehat{A}_{p_0^*}})\widehat{\Sigma})+\mathrm{tr}((P_{\widehat{B}_{q_0}}\otimes P_{\widehat{A}_{p_0}})\widehat{\Sigma})$ $-2\mathrm{tr}((P_{\widehat{B}_{q_0\wedge q_0^*}}\otimes P_{\widehat{A}_{(p_0\wedge p_0^*)}})\widehat{\Sigma})+O_P(n^{-1/2})$, to which (2.8) can be applied to obtain

$$A_{1n} = \mathrm{tr}([I_{p_0^*q_0^*}-(B^{\top}P_{B_{q_0}}B)\otimes(A^{\top}P_{A_{p_0}}A)]\Sigma_{\mathrm{vec}(U)}) \tag{2.10}$$

$$+\sigma^2(p_0^*q_0^* + p_0q_0 - 2(p_0^* \wedge p_0)(q_0^* \wedge q_0)) + O_P(n^{-1/2}).$$

By the assumption $c > \sigma^2$, $\Sigma_{\mathrm{vec}(U)} - \sigma^2 I_{p_0^*q_0^*}$ is positive definite. By von Neumann's trace inequality (cf. [10]),

$$\begin{aligned}(2.11)\quad \text{1st summand in (2.10)} &\geq \mathrm{tr}(\{I_{p_0^*q_0^*} - (B^\top P_{\widehat{B}_{q_0}} B) \otimes (A^\top P_{\widehat{A}_{p_0}} A)\}\sigma^2 I_{p_0^*q_0^*}) \\ &= \sigma^2(p_0^*q_0^* - (p_0^* \wedge p_0)(q_0^* \wedge q_0)).\end{aligned}$$

In the first inequality of (2.11), "=" holds only when $p_0 \geq p_0^*$ and $q_0 \geq q_0^*$. Note that $I_{p_0^*q_0^*} - (B^\top P_{\widehat{B}_{q_0}} B) \otimes (A^\top P_{\widehat{A}_{p_0}} A)$ is symmetric and nonnegative definite. By (2.10) and (2.11),

$$(2.12)\qquad A_{1n} = \sigma^2(2p_0^*q_0^* + p_0q_0 - 3(p_0^* \wedge p_0)(q_0^* \wedge q_0)) + O_P(n^{-1/2}).$$

Moreover, A_{3n} in (2.7) is equal to

$$\begin{aligned}&\frac{2(n-1)\sigma^2}{n}(p_0q_0 - p_0^*q_0^*) + \frac{2\sigma^2}{n}\left[\sum_{j=1}^{p_0}\sum_{\ell=p_0+1}^{p}\frac{\widehat{\lambda}_j + \widehat{\lambda}_\ell}{\widehat{\lambda}_j - \widehat{\lambda}_\ell} + \sum_{j=1}^{q_0}\sum_{\ell=q_0+1}^{q}\frac{\widehat{\xi}_j + \widehat{\xi}_\ell}{\widehat{\xi}_j - \widehat{\xi}_\ell}\right] \\ &- \frac{2\sigma^2}{n}\left[\sum_{j=1}^{p_0^*}\sum_{\ell=p_0^*+1}^{p}\frac{\widehat{\lambda}_j + \widehat{\lambda}_\ell}{\widehat{\lambda}_j - \widehat{\lambda}_\ell} + \sum_{j=1}^{q_0^*}\sum_{\ell=q_0^*+1}^{q}\frac{\widehat{\xi}_j + \widehat{\xi}_\ell}{\widehat{\xi}_j - \widehat{\xi}_\ell}\right],\end{aligned}$$

which can be combined with (2.9), (2.12) and (2.6) to yield

$$\begin{aligned}(2.13)\quad &\mathrm{S}_u^{(n)}(p_0, q_0; \sigma^2) - \mathrm{S}_u^{(n)}(p_0^*, q_0^*; \sigma^2) \geq \sigma^2(p_0q_0 - (p_0^* \wedge p_0)(q_0^* \wedge q_0)) \\ &+ \frac{2\sigma^2}{n}\left[\sum_{j=1}^{p_0}\sum_{\ell=p_0+1}^{p}\frac{\widehat{\lambda}_j + \widehat{\lambda}_\ell}{\widehat{\lambda}_j - \widehat{\lambda}_\ell} + \sum_{j=1}^{q_0}\sum_{\ell=q_0+1}^{q}\frac{\widehat{\xi}_j + \widehat{\xi}_\ell}{\widehat{\xi}_j - \widehat{\xi}_\ell}\right] \\ &- \frac{2\sigma^2}{n}\left[\sum_{j=1}^{p_0^*}\sum_{\ell=p_0^*+1}^{p}\frac{\widehat{\lambda}_j + \widehat{\lambda}_\ell}{\widehat{\lambda}_j - \widehat{\lambda}_\ell} + \sum_{j=1}^{q_0^*}\sum_{\ell=q_0^*+1}^{q}\frac{\widehat{\xi}_j + \widehat{\xi}_\ell}{\widehat{\xi}_j - \widehat{\xi}_\ell}\right] + O_P(n^{-1/2}).\end{aligned}$$

Note that

$$\sum_{j=1}^{p_0}\sum_{\ell=p_0+1}^{p}\frac{\widehat{\lambda}_j + \widehat{\lambda}_\ell}{\widehat{\lambda}_j - \widehat{\lambda}_\ell} - \sum_{j=1}^{p_0^*}\sum_{\ell=p_0^*+1}^{p}\frac{\widehat{\lambda}_j + \widehat{\lambda}_\ell}{\widehat{\lambda}_j - \widehat{\lambda}_\ell} = \sum_{j=p_0^*+1}^{p_0}\sum_{\ell=j+1}^{p}\frac{\widehat{\lambda}_j + \widehat{\lambda}_\ell}{\widehat{\lambda}_j - \widehat{\lambda}_\ell} \geq 0 \ \text{ if } p_0 > p_0^*;$$

$$\sum_{j=1}^{q_0}\sum_{\ell=q_0+1}^{q}\frac{\widehat{\xi}_j + \widehat{\xi}_\ell}{\widehat{\xi}_j - \widehat{\xi}_\ell} - \sum_{j=1}^{q_0^*}\sum_{\ell=q_0+1}^{q}\frac{\widehat{\xi}_j + \widehat{\xi}_\ell}{\widehat{\xi}_j - \widehat{\xi}_\ell} = \sum_{j=q_0^*+1}^{q_0}\sum_{\ell=j+1}^{q}\frac{\widehat{\xi}_j + \widehat{\xi}_\ell}{\widehat{\xi}_j - \widehat{\xi}_\ell} \geq 0 \ \text{ if } q_0 > q_0^*.$$

On the other hand, if $p_0 < p_0^*$ (respectively, $q_0 < q_0^*$), $(\widehat{\lambda}_j + \widehat{\lambda}_\ell)/(\widehat{\lambda}_j - \widehat{\lambda}_\ell)$ (respectively, $(\widehat{\xi}_j + \widehat{\xi}_\ell)/(\widehat{\xi}_j - \widehat{\xi}_\ell)$) is positive and bounded away from 0 for $j \le p_0$ and $\ell > p_0$ (respectively, $j \le q_0$ and $\ell > q_0$). Thus, we obtain from (2.13) that

$$\mathrm{S}_u^{(n)}(p_0, q_0; \sigma^2) - \mathrm{S}_u^{(n)}(p_0^*, q_0^*; \sigma^2) \ge \sigma^2(p_0 q_0 - (p_0^* \wedge p_0)(q_0^* \wedge q_0)) + O_P(n^{-1/2}),$$

with equality only when $p_0 \ge p_0^*$ and $q_0 \ge q_0^*$, from which it follows that as $n \to \infty$,

(2.14)
$$\mathrm{S}_u^{(n)}(p_0, q_0; \sigma^2) - \mathrm{S}_u^{(n)}(p_0^*, q_0^*; \sigma^2) \begin{cases} = 0 & \text{if } p_0 = p_0^* \text{ and } q_0 = q_0^* \\ > o_P(1) & \text{otherwise.} \end{cases}.$$

In (2.14), "$s_n > o_P(1)$" means that given $\varepsilon > 0$ and $\delta > 0$, there exists $n_{\varepsilon,\delta}$ such that $\mathrm{P}(s_n > \varepsilon) \ge 1 - \delta$ for $n \ge n_{\varepsilon,\delta}$, which completes the proof. □

Since (p_0^*, q_0^*) and $P_{B_{q_0^*} \otimes A_{p_0^*}}$ can be consistently estimated in the first stage of 2SDR, we can apply the consistency of $\widehat{r}_{\mathrm{GIC}}$ established by Hung et al. [19] for PCA models to obtain the following.

Corollary. *Assume that the* $\mathrm{H_M PCA}$ *model holds and* $c > \sigma^2$. *Suppose that* $r^* \le r_u$. *Then* $\mathrm{P}(\widehat{r}_{\mathrm{GIC}} = r^*) \to 1$ *as* $n \to \infty$.

2.2 Simulation study of performance

Table 1(a) (respectively, Table 1(b)) summarizes the results, each of which is based on 100 simulation replications, of a simulation study of the performance of 2SDR in the PCA model (respectively, the $\mathrm{H_M PCA}$ model). Note that if the actual ranks p_0^*, q_0^* and r^* are all known, 2SDR has computational complexity of the order $O(p^2 p_0^* + q^2 q_0^*) + O((p_0^* q_0^*)^2 r^*)$, in which the first summand is that of MPCA, in contrast to $O(p^2 q^2 r)$ for PCA that vectorizes the image without going through MPCA first. Table 1(a) assumes that the data are generated from the PCA model (1.1) with $y = \mathrm{vec}(X)$ and $pq \times r^*$ random matrix Γ with orthonormal columns,

$$p = q = 40, r^* = 25; \mu = 0, c^{-1}\varepsilon \sim N(0, I_{pq}), \nu \sim N(0, \Delta), \tag{2.15}$$

where $\Delta = \mathrm{diag}(\delta_1, \delta_2, \cdots, \delta_{r^*})$ with $\delta_i = 10(26 - i)$, and the value of c is listed in Table 1(a) alongside the sample size n used to fit the model. Note that this choice of relatively small p, q and r^* makes fitting the PCA model computationally feasible. We apply the SURE criterion for fitting MPCA model which is incompatible with the data generating mechanism (2.15), and we get $\widehat{p}_0 = \widehat{q}_0 = 1$

in all 100 simulations. Although the SURE criterion fails to choose a reasonable rank, we still carry out MPCA and 2SDR by assuming that nominal values of $p_0 = q_0 = 10$ in running 100 simulations of the (wrong) working model and the actual values $r^* = 25$. However, although 2SDR starts with the wrong working model when the data are generated from the PCA model (1.1), what really matters is the performance of image reconstruction, and fitting working models to a sample of size n and dimension reduction are means to that end. A commonly used performance measure in image reconstruction is the Mean Squared Error (MSE)$= \sum_{i=1}^{n} \|\text{vec}(\widehat{X}_i) - \text{vec}(\text{true image})\|^2/(pqn)$, where $\widehat{X}_i$ is the reconstructed image. Table 1(a) gives the simulation results of MSE for 2SDR, in comparison with fitting the PCA model that generates the data and with fitting the wrong MPCA model. The four settings in Table 1(a) cover two sample sizes $(n = 1000, 100)$ and two signal-to-noise ratios (SNR= 0.5, 0.1, corresponding to $c = 4, 20$) defined by $E(||\Gamma\nu||^2)/(pqc)$. It shows that 2SDR has MSE comparable to PCA for $n = 100$ and has about $1/2$ of the MSE of PCA for $(n, c) = (100, 20)$. Table 1(b) assumes that the data are generated from the H_MPCA model with

(2.16)

$$p = q = 50, p_0^* = q_0^* = 8, \sigma^{-1}\text{vec}(\mathscr{E}) \sim N(0, I_{pq}) \text{ for its MPCA component,}$$
$$r^* = 8, c^{-1}\varepsilon \sim N(0, I_{p_0^* q_0^*}) \text{ and } c = 1.001\sigma^2 \text{ for subsequent PCA component,}$$

Table 1: MSE, with standard deviation in parentheses, of PCA, MPCA and 2SDR.

(a) Data generated from PCA model (2.15).

	PCA	MPCA	2SDR	PCA	MPCA	2SDR
c \ n	1000			100		
4	0.1831 (0.0011)	1.9851 (0.0172)	1.8070 (0.0172)	1.2297 (0.0089)	2.0951 (0.0562)	1.9694 (0.0562)
20	1.1695 (0.0078)	3.1956 (0.0199)	2.2868 (0.0188)	6.8777 (0.0461)	3.8893 (0.0585)	3.1972 (0.0576)

(b) Data generated from H_MPCA model (2.16).

	PCA	MPCA	2SDR	PCA	MPCA	2SDR
σ^2 \ n	1000			100		
1.1	0.0174 (0.0001)	0.0578 (0.0003)	0.0089 (0.0001)	0.1105 (0.0011)	0.0705 (0.0010)	0.0255 (0.0001)
5.6	0.0937 (0.0008)	0.2947 (0.0016)	0.0457 (0.0005)	0.6150 (0.0073)	0.3662 (0.0057)	0.1363 (0.0031)

Table 2: Accuracy rates of $\widehat{r}_{\text{GIC}}$, AIC and BIC

	SNR = 0.5			SNR = 0.1		
	AIC	BIC	$\widehat{r}_{\text{GIC}}$	AIC	BIC	$\widehat{r}_{\text{GIC}}$
Gaussian	0.96	1.00	1.00	0.98	1.00	1.00
T_5	0.00	0.85	0.97	0.00	0.82	0.93

in which $\kappa_i = 40(9-i)$, with $1 \le i \le r^*$, A (respectively, B) is a $p \times p_0^*$ (respectively, $q \times q_0^*$) matrix with orthonormal columns, which are the eigenvectors of the ordered eigenvalues of $(X-M)P_B(X-M)^\top$ (respectively, $(X-M)P_A(X-M)^\top$); see the second paragraph of Section 1.3. The four settings in Table 1(b) cover two sample sizes $(n = 1000, 100)$ and two signal-to-noise ratios (SNR= 0.5 corresponding to σ^2= 1.1, 0.1 corresponding to σ^2= 5.6); here SNR $=\{\sum_{i=1}^{r^*}(\kappa_i - c)\}/(pq\sigma^2 + p_0^* q_0^* c)$. Table 1(b) shows that 2SDR outperforms both MPCA and PCA in all settings, particularly for relatively small sample size $n = 100$ or low SNR ratio $= 0.1$.

We next conduct a simulation study of the accuracy ratio of $\widehat{p}_0, \widehat{q}_0$ using the SURE criterion under the H_MPCA model for $n = 1000$ and $\sigma^2 = 1.1, 5.6$, not only for the Gaussian model for $\sigma^{-1}\text{vec}(\mathscr{E})$ and $c^{-1}\varepsilon$ but also for the non-Gaussian case $\sigma^{-1}\text{vec}(\mathscr{E}) \sim T_5$ and $c^{-1}\varepsilon \sim T_5$, where T_5 is the pq-dimensional (or $p_0^* q_0^*$-dimensional, for $c^{-1}\varepsilon$) t-distribution with 5 degree of freedom. All of the 100 simulations give $(\widehat{p}_0, \widehat{q}_0) = (p_0^*, q_0^*)$. We then consider the accuracy rate $\text{P}(\widehat{r}_{\text{GIC}} = r^*)$ in the PCA stage of 2SDR and compare it with AIC and BIC that assume p_0^*, q_0^* to be known. The results are given in Table 2 and show that $\widehat{r}_{\text{GIC}}$ has marked improvement over AIC and BIC in the non-Gaussian case of T_5.

3 Cryo-EM applications

In this section we apply 2SDR to the analysis of cryo-EM benchmark datasets in Sections 3.2 and 3.3 dealing with 70s Ribosome and 80s Ribosome. A ribosome is made from complexes of RNAs (ribonucleic acids) that are present in all living cells to perform protein synthesis by linking amino acids together in the order specified by the codons of mRNA (messenger RNA) molecules to form polypeptide chains. A 70s Ribosome comprises of a large 50s subunit and small 30s subunit; the "s" stands for Svedberg, a unit of time equal to 10^{-13} seconds, measuring how fast molecules move in a centrifuge. Eukaryotic ribosomes are also known as 80s Ribosomes and have a large 60s subunit and small 40s subunit.

In a cell or a virus, biological processes are carried out by numerous nanomachines made of protein complexes. When the structures of these protein ma-

chines are visualized, they go through a series of functionally relevant conformations along the time trajectory. Because the protein sample for a cryo-EM experiment is under an almost physiological environment, it usually collects various conformations of the protein structure. However, a homogeneous conformation dataset is a basic requirement to push high resolution of the 3D density map. Thus, 2D clustering which aims to separate the data into subsets of homogeneous conformation has become an effective approach in cryo-EM data analysis [21, 28, 31]. In the past decade, the linear subspace model that represents the protein motion using the eigenvolumes from the covariance matrix of 3D structures is an active research area. This technique not only can analyze discrete heterogeneity [21, 28], but can also obtain energy landscape associated with the 3D structures [3, 16, 17]. In all these approaches, PCA plays an important role to estimate the top eigenvolumes. However, volume vectorization may produce enormous dimensionality and the traditional solution by voxel binning usually results in blurring of the variations among groups and degrading the clustering performance [3]. Section 3.1 uses a heterogeneous dataset of 2D cryo-EM images to analyze the 3D variability of the reconstructed images.

3.1 3D variability analysis using a heterogeneous dataset of 2D images

We follow [28] to generate a dataset containing 9,453 2D particle images projected from five 70S Ribosome conformations with minor differences due to combinations of the absence or presence of tRNA (transfer RNA) and EFG (elongation factor G). Next, we resampled these particle images to generate 11,000 3D volumes (density maps) on $75 \times 75 \times 75$ voxels. We then solve the eigenvolumes using PCA or 2SDR,[4] and compare the performance of these two methods using the factorial coordinates defined in [28].

As shown in Figure 2, more broken portions appear in the eigenvolumes solved by PCA, which suggests that the eigenvolumes solved by 2SDR is more reliable. This is confirmed by the t-SNE plots and k-means with 5 classes on their factorial coordinates. Since each particle image corresponds to a projection of one of the five conformations, we expect to see five clusters among the factorial coordinates of all the particle images. The t-SNE plot can separate 5 groups better for 2SDR approach than that for PCA as shown in Figure 2. The clustering performance is also quantitatively evaluated through impurity and c-impurity [25] defined as follows. Let $\{c_i\}$ be sets of true class labels, $\{w_j\}$ be sets of predicted cluster

[4] To perform 2SDR, the rank of each mode for the first stage is set to 80% of explain variance ratio; the rank for the second stage is 8 suggested by the elbow method of the scree plot.

labels, and $|.|$ be the cardinality of the set. The impurity and c-impurity are defied as

$$\text{impurity} = 1 - n^{-1} \sum_j \max_i |c_i \cap w_j|$$
$$\text{c-impurity} = 1 - n^{-1} \sum_i \max_j |c_i \cap w_j|$$

The impurity is 0 if each predicted cluster contains only members of a single class. The c-impurity is 0 if all members of a given class label are assigned to the same predicted cluster. In summary, small values of the impurity and c-impurity indicate better performance of the clustering results. The impurity and c-impurity numbers are 0.01 for 2SDR whereas those for PCA are 0.1995 and 0.2413, respectively, showing the superiority of 2SDR in dimension reduction for 3D density maps.

3.2 Performance measure and applications to 70s Ribosome data

Here, we apply our algorithm and the rank selection procedure on the synthetic cryo-EM data in this subsection where the dataset is prepared as follows. We first downloaded the Relion [30] classification benchmark dataset, E. coli 70s Ribosome, which contains 10000 particle images with box size 130×130. The first 5000 and the second 5000 images of this dataset represent different structure conformations. Second, we apply CryoSparc [29] to generate the 3D density map from the first 5000 images referred to the Ribosome bound with an elongation factor (EF-G). Then, a total of 50 distinct 2D images with 130×130 pixels were generated by projecting the 3D density map in equally spaced (angle-wise) orientations. Third, 5000 images were generated from these 50 projections.[5] Each image was then convoluted with the electron microscopy contrast transfer function randomly sampled from a set of 50 CTF values.[6] Finally, i.i.d. Gaussian noise $N\left(0, \sigma^2 I_{pq}\right)$ with different σ^2 is added to generate 3 datasets such that the SNR is equal to 0.09, 0.06 and 0.03, respectively.

Quantitative comparison on five dimension reduction or denoising methods including PCA, MPCA, 2SDR, Wavelet [8] and BM3D [12] are then conducted on the synthetic dataset. MSE and Peak Signal to Noise Ratio (PSNR) are computed

[5] Here, to reflect the fact that real data is often collected with preferred orientations, 10 projections are repeated with 400 copies and the other projections are repeated with 25 copies.

[6] Here, the defocus is randomly sampled from 2.1um to 3.5um and the astigmatism angle is from 0.2 to 1.4 radian. The electron beam accelerating voltage was set to be 300KeV with spherical aberration Cs = 2mm, amplitude contrast=0.07 and pixel size is 2.82Å.

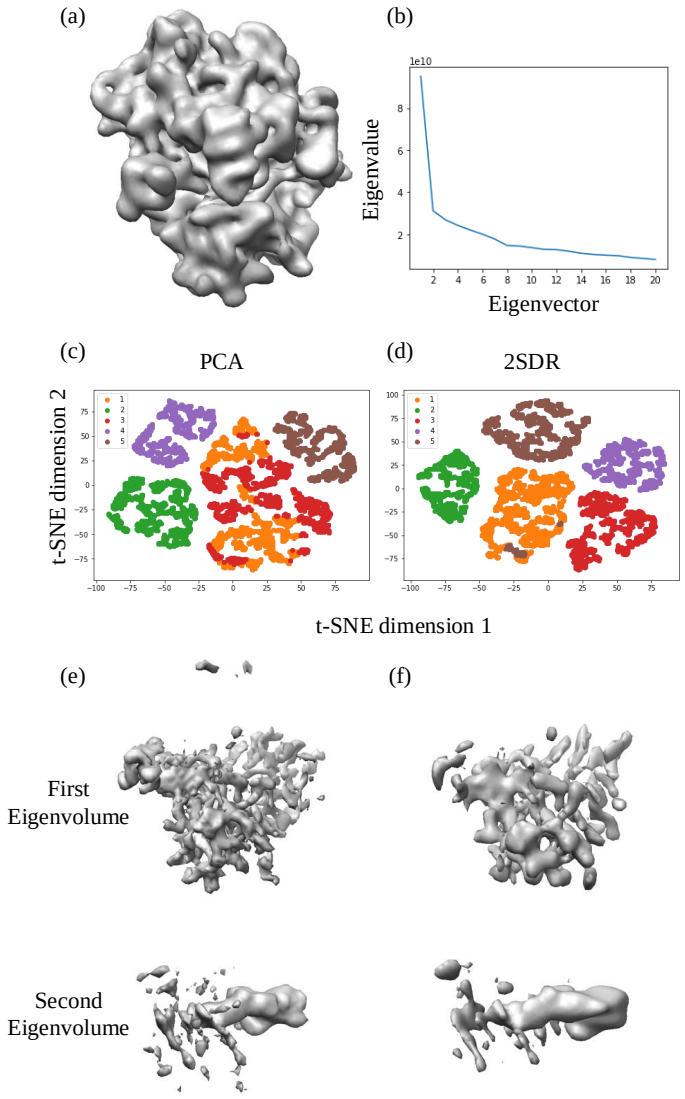

Figure 2: 3D variability analysis. (a) The average volume. (b) The Scree plot that shows leading 20 eigenvalues. (c)(d) The scatter plot of t-SNE embedding of 8 factorial coordinates computed by PCA and 2SDR approaches and the color labels are according to the class assignments by k-means. (e) The first and second eigenvolume solved by performing PCA on 11,000 resampled volumes. (f) Same as (e) but with 2SDR.

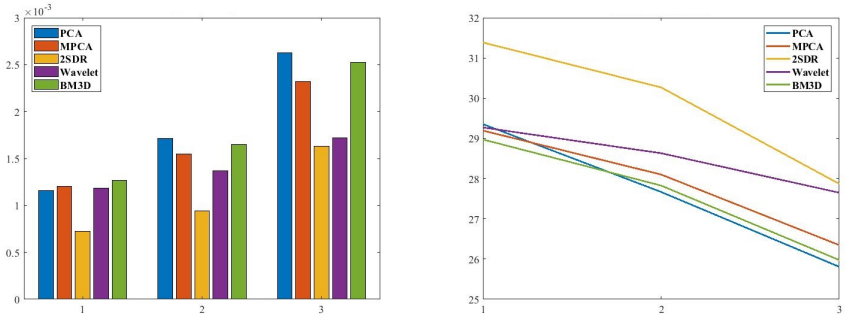

(a) (b)

Figure 3: (a) MSE and (b) PSNR of synthetic E. coli 70s Ribosome dataset using PCA, MPCA, 2SDR, Wavelet and BM3D. Three simulations under different settings are tested: Label 1 for SNR $= 0.09$; Label 2 for SNR $= 0.06$; Label 3 for SNR $= 0.03$. The details results of each setting are in the Table 3.

Table 3: MSE and PSNR comparison for various dimension reduction methods on synthetic E. coli 70s Ribosome dataset.

Method	PCA	MPCA	2SDR	Wavelet	BM3D
Parameters	Setting 1 : SNR $= 0.09$				
MSE (10^{-3})	1.1435	1.2040	0.7268	1.1825	1.2669
Std of MSE (10^{-5})	0.4056	0.0985	0.0490	0.0748	0.0501
PSNR	29.4176	29.1939	31.3860	29.2718	28.9727
Std of PSNR (10^{-1})	0.1540	0.0356	0.0295	0.0274	0.0173
	Setting 2 : SNR $= 0.06$				
MSE (10^{-3})	1.7109	1.5484	0.9402	1.3703	1.6493
Std of MSE (10^{-5})	0.5474	0.1323	0.0742	0.1034	0.1609
PSNR	27.6679	28.1010	30.2676	28.6319	27.8270
Std of PSNR (10^{-1})	0.1390	0.0371	0.0344	0.0328	0.0424
	Setting 3 : SNR $= 0.03$				
MSE (10^{-3})	2.6263	2.3199	1.6331	1.7182	2.5267
Std of MSE(10^{-5})	0.5925	0.2107	0.1315	0.1616	0.2536
PSNR	25.8066	26.3453	27.8698	27.6493	25.9744
Std of PSNR (10^{-1})	0.0980	0.0395	0.0349	0.0409	0.0436

based on 100 replica simulation with three SNR levels, where PSNR is defined as

$$\text{PSNR}(X_i, \widehat{X}_i) = 10 \times \log_{10} \frac{\text{Range}(X_i)^2}{\text{MSE}}, \tag{3.1}$$

where $\text{Range}(X_i)$ is the value range according to the datatype of X_i.[7] MSE and PSNR in Figure 3 show that 2SDR outperforms all the other methods. The images reconstructed by these methods are presented in Figure 4, where the SNR is decreased from left-hand side to right-hand side. When SNR is 0.09, all methods can reconstruct the particles well. As the noise increases, Figure 4 shows that the particles reconstructed by 2SDR and PCA match the original images much better than those by MPCA, Wavelet and BM3D. When SNR drops to 0.03, 2SDR performs better than PCA in regarding to the contrast and background noise reduction. We further apply t-SNE on the scores solved by PCA, MPCA and 2SDR at SNR$=0.03$ in Figure 5 and observe that MPCA and 2SDR can perfectly separate the 50 clusters of the synthetic dataset while PCA tends to have small groups aggregate together. Overall speaking, 2SDR performs the best and can prepare the data best for clustering.

After the encouraging results obtained from the synthetic dataset, we proceed to test 2SDR on experiment dataset. The first 5000 particle images from the 70s Ribosome dataset are used for demonstration, where Sparx [18] package for alignment. To implement the rank selection procedure introduced in Section 2.1, we choose (p_u, q_u) as the 35% of total variance on both column and row spaces. We present the reconstructed images of 9 randomly selected particles by PCA, MPCA, 2SDR, Wavelet and BM3D in Figure 6. MPCA, Wavelet and BM3D do not perform well in presenting the particle shapes on this real dataset.

We apply t-SNE on the scores solved by PCA, MPCA and 2SDR.[8] Figure 7 shows that PCA and 2SDR can better separate the groups representing different orientated projections. The γ-SUP is further applied on the scores to evaluate the performance. Since γ-SUP is insensitive to the parameter s, we set it to a small value $s = 0.025$ as suggested in the original paper [9]. The scale parameter τ is selected using phase transition plot as follows. We first normalize the scores and set an upper bound τ such that γ-SUP groups all points into one cluster. Second, we recursively divide the τ by 2 until each points forms one cluster and record it as the lower bound. Finally, we perform the grid search between the upper and lower bound and select the τ that maximizes the cluster number with the condition that each cluster is larger than a prescribed size. γ-SUP shows that 2SDR can produce

[7] For instance, if the data type of image is unit8 then it is 255.

[8] Here, the images are aligned using multireference alignment [18] for better visualization.

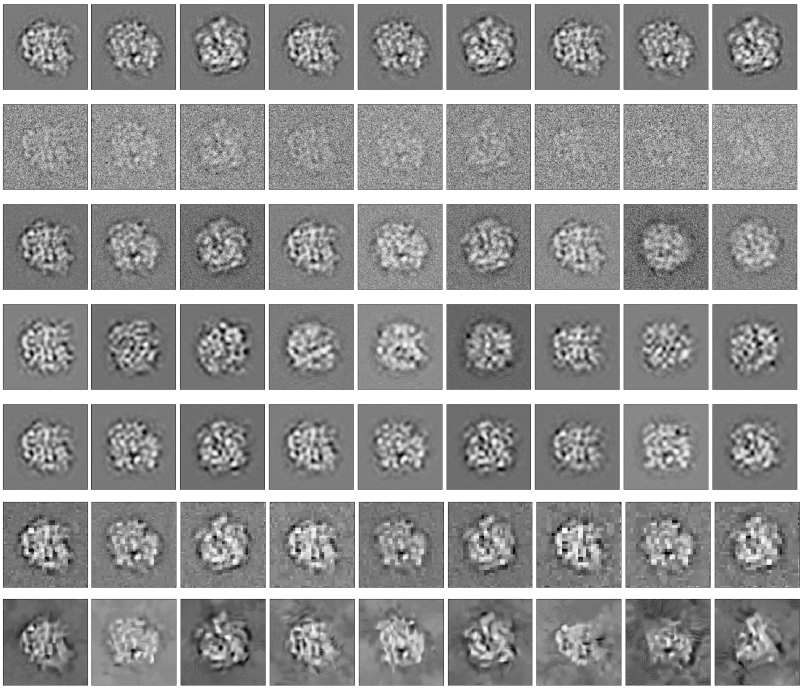

Figure 4: Reconstruction of synthetic 70s Ribosome images by 5 dimension reduction methods. The first row shows the 9 original clean synthetic images. The second row shows the noisy images corresponding to different SNR levels; the first 3 columns from the left correspond to SNR$=0.09$, the middle 3 columns correspond to SNR$=0.06$ and the last 3 columns correspond to SNR$=0.03$. The third row is the result by applying PCA to the second row with $\widehat{r}_{\text{GIC}} = 53$ (first 3 images from the left), $\widehat{r}_{\text{GIC}} = 48$ (middle 3 images) and $\widehat{r}_{\text{GIC}} = 33$ (last 3 images). The fourth row is the result by applying MPCA with $(\widehat{p}_0, \widehat{q}_0) = (15, 15)$ for the first 3 images from the left, $(14, 14)$ for the middle 3 images, and $(11, 11)$ for the last 3 images. The fifth row is the result by applying 2SDR, with the same choice of $(\widehat{p}_0, \widehat{q}_0)$ as in MPCA followed by that of $\widehat{r}_{\text{GIC}} = 53,\ 48,\ 33$. The sixth (respectively, seventh) row gives the result by applying Wavelet (respectively, BM3D).

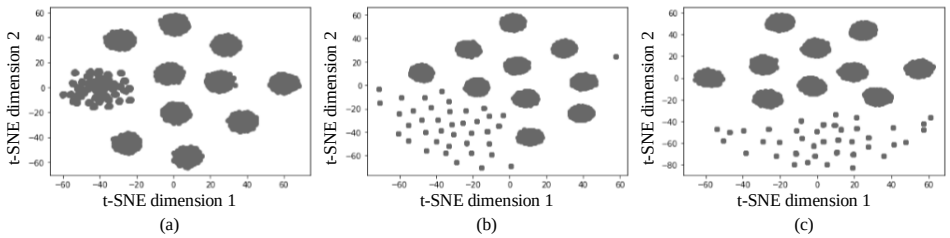

Figure 5: t-SNE embedding of (a) PCA, (b) MPCA and (c) 2SDR at SNR$=0.03$ on synthetic E. coli 70s Ribosome dataset.

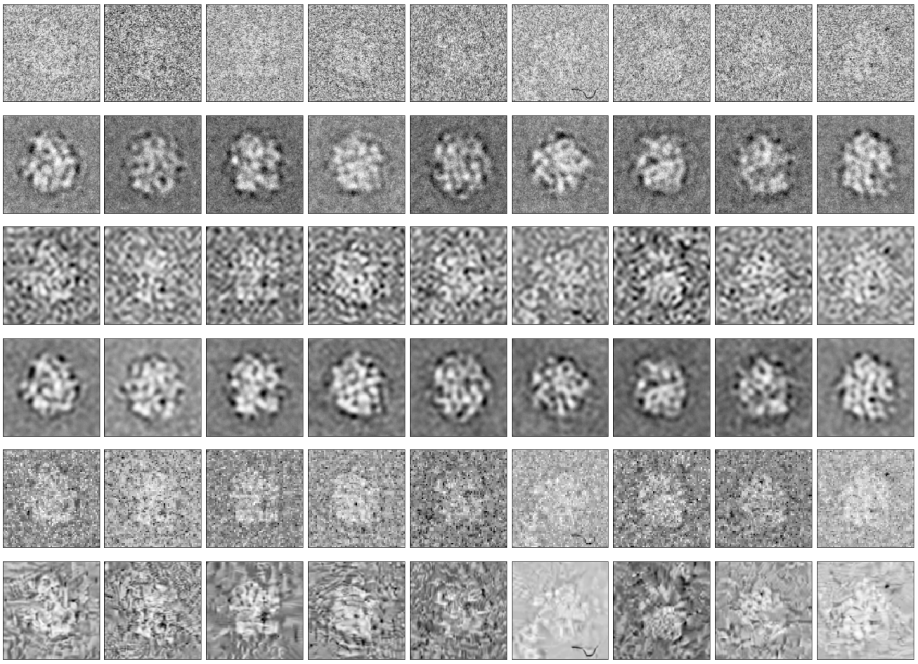

Figure 6: Reconstruction of experiment E. coli 70s Ribosome particle images by 5 dimension reduction methods. The first row shows the 9 original particle images. The second row is by PCA with $\widehat{r}_{\text{GIC}} = 60$ components. The third row is by MPCA with $(\widehat{p}_0, \widehat{q}_0) = (25, 25)$, which contributes 625 basis components. The fourth row is by 2SDR: $(\widehat{p}_0, \widehat{q}_0) = (25, 25)$ for MPCA followed by choosing $\widehat{r}_{\text{GIC}} = 60$ for PCA. The fifth row is by Wavelet denoising and the sixth row is by BM3D.

the largest number of good classes and the class averages from PCA and 2SDR show more structural details in Figure 7 .

3.3 Relion 80s Ribosome benchmark dataset

To further demonstrate the computational advantage of 2SDR on large dataset, we test 80s Ribosome that comes from Relion Benchmark example. This dataset contains 105,247 particle images with pixel size 360 by 360 that many current PCA implementations fail to solve the complete set of eigenvectors due to the limitation of the underlying numerical linear algebra package LAPACK [4].[9] In contrast, we can perform 2SDR in the server since the computational complexity

[9] We used a server equipped with two Intel Xeon CPU E5-2699 v4 at 2.20GHz and 512GB memory to execute PCA for this dataset.

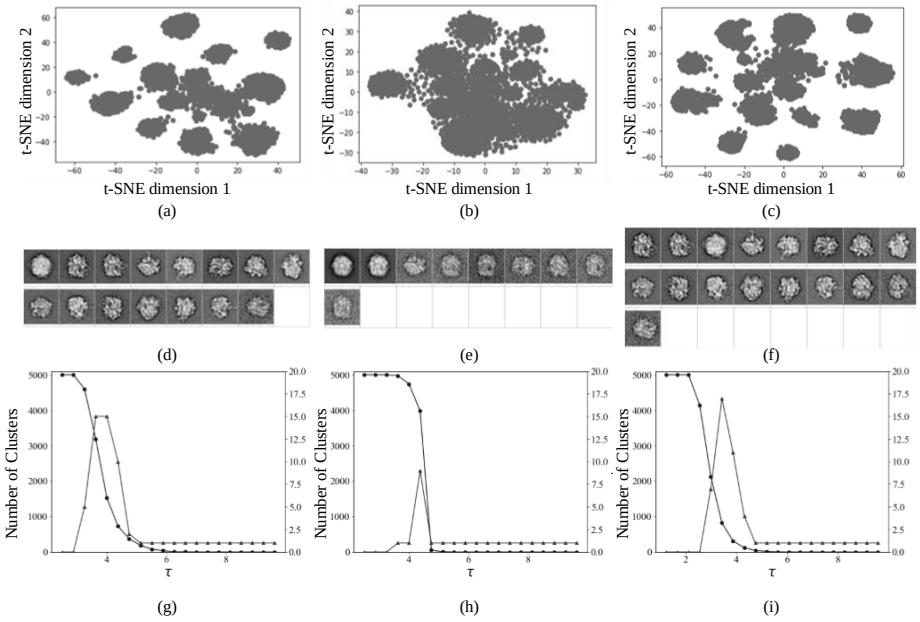

Figure 7: (a),(b),(c) from left to right, contains three t-SNE plots of the scores generated by PCA, MPCA and 2SDR; (d),(e),(f) presents the class averages output by the clustering algorithm γ-SUP of PCA, MPCA and 2SDR; (g),(h),(i) shows the transition plot of γ-SUP on the experiment E. coli 70s Ribosome dataset. In (g),(h),(i), the left scale bar corresponds to circle marker, which is the number of clusters, and the right scale bar corresponds to triangle marker, which is the number of clusters with cluster size larger than 10.

has been reduced by several orders of magnitude. Figure 8 shows nine randomly selected images and their reconstructions by MPCA, 2SDR, Wavelet and BM3D; 2SDR clearly performs much better than the other methods.

4 Discussion

PCA was introduced in the early development of single particle cryo-EM analysis to reduce the dimension of the 2D projection images to facilitate 2D image clustering [14, 38]. Recently Amit Singer and his coauthors [7, 43, 44] introduced a method called ”steerable PCA” to deal with the random orientation nature of 2D projection images by including all possible rotated 2D projections into the data covariance matrix to yield promising outcomes on particle denoising. PCA has more

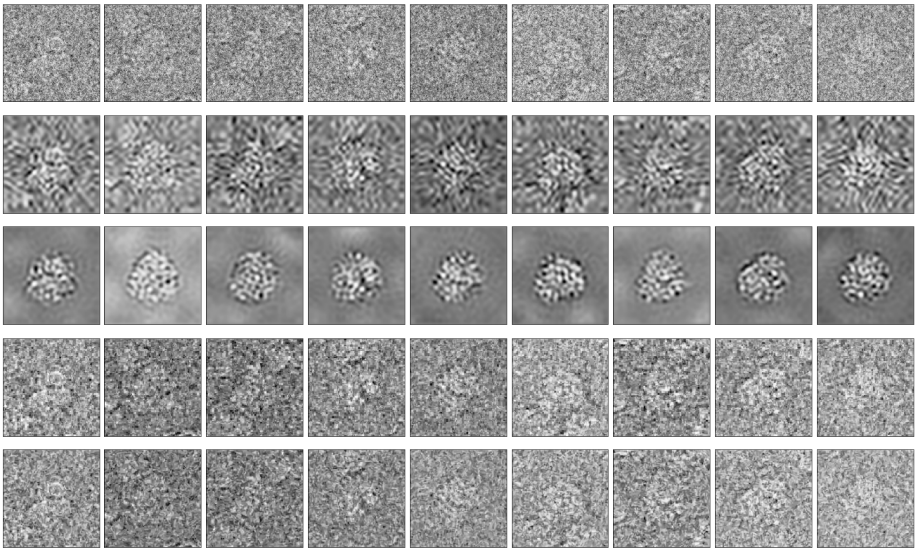

Figure 8: Reconstruction of 9 randomly selected 80s Ribosome particle images: first row shows the original images, second row the MPCA reconstruction with $(\widehat{p}_0, \widehat{q}_0) = (26, 26)$, third row the 2SDR reconstruction with $(\widehat{p}_0, \widehat{q}_0) = (26, 26)$ and $\widehat{r}_{\text{GIC}} = 152$, fourth row the Wavelet reconstruction, and fifth row the BM3D reconstruction.

general applications in cryo-EM analysis [1, 39] such as analyzing discrete heterogeneity [21, 28] and obtaining energy landscape associations with 3D structures [3, 16, 17]. A disadvantage of applying PCA to these tensor structure data lies in its computational bottleneck.

Many current statistical algorithms are designed for vector data. To handle matrix data or high-order tensor data, a naive approach is to accommodate the input format requirement by data vectorization, which can have prohibitive computational cost. We have shown that 2SDR can overcome this computational difficulty and yet have superior performance over PCA. In addition, H_MPCA can be readily extended to a mixture model of the form

$$\begin{aligned} X \mid z &= M + A(U_z)B^\top + \mathscr{E} \\ \text{vec}(U_z) &= \mu_z + G\nu + \varepsilon, \;\; z \in \{1, \ldots, K\}, \end{aligned}$$

where we introduce a random variable z for cluster label and μ_z is the mean of $\text{vec}(U_z)$, $P(z = k) = \pi_k$, $k \in \{1, ..., K\}$ and $\sum_{k=1}^{K} \pi_k = 1$. We have recently applied this extension to cryo-EM image analysis and found excellent performance, and

the promising results have led to further development of this idea as our ongoing project. Moreover, 2SDR is not limited to the 2D cryo-EM image analysis. We have also demonstrated 2SDR provides a promising alternative to PCA with better performance and less computational overhead in the 3D heterogeneous volume analysis. In conclusion, 2SDR is a powerful innovation that can provide an alternative to PCA for dimension reduction in the analysis of noisy high-dimensional data.

References

[1] Afanasyev, P., Seer-Linnemayr, C., Ravelli, R. B., Matadeen, R., De Carlo, S., Alewijnse, B., Portugal, R. V., Pannu, N. S., Schatz, M. and van Heel, M. (2017). Single-particle cryo-EM using alignment by classification (ABC): the structure of Lumbricus terrestris haemoglobin. *IUCrJ* **4** 678–694.

[2] Amari, S. and Ohara, A. (2011). Geometry of q-exponential family of probability distributions. *Entropy* **13** 1170-1185.

[3] Andén, J. and Singer, A. (2018). Structural variability from noisy tomographic projections. *SIAM Journal on Imaging Sciences* **11** 1441–1492.

[4] Anderson, E., Bai, Z., Bischof, C., Blackford, S., Dongarra, J., Du Croz, J., Greenbaum, A., Hammarling, S., McKenney, A. and Sorensen, D. (1999). *LAPACK Users' guide* **9**. SIAM.

[5] Bai, Z., Choi, K. P. and Fujikoshi, Y. (2018). Consistency of AIC and BIC in estimating the number of significant components in high-dimensional principal component analysis. *The Annals of Statistics* **46** 1050–1076.

[6] Belkin, M. and Niyogi, P. (2003). Laplacian eigenmaps for dimensionality reduction and data representation. *Neural Computation* **15** 1373–1396.

[7] Bhamre, T., Zhang, T. and Singer, A. (2016). Denoising and covariance estimation of single particle cryo-EM images. *Journal of Structural Biology* **195** 72–81.

[8] Chang, S. G., Yu, B. and Vetterli, M. (2000). Adaptive wavelet thresholding for image denoising and compression. *IEEE Transactions on Image Processing* **9** 1532–1546.

[9] Chen, T.-L., Hsieh, D.-N., Hung, H., Tu, I.-P., Wu, P.-S., Wu, Y.-M., Chang, W.-H. and Huang, S.-Y. (2014). γ-SUP: A Clustering Algorthm for Cryo-Electron Microscopy Images of Asymmetric Particles. *The Annals of Applied Statistics* **8** 259-285.

[10] Chretien, S. and Wei, T. (2015). Von Neumann's trace inequality for tensors. *Linear Algebra and its Applications* **482** 149–157.

[11] Chung, F. R. K., Grigoryan, A. and Yau, S. T. (2000). Higher eigenvalues and isoperimetric inequalities on Riemannian manifolds and graphs. *Communications on Analysis and Geometry* **8** 969–1026.

[12] Dabov, K., Foi, A., Katkovnik, V. and Egiazarian, K. (2007). Image denoising by sparse 3-D transform-domain collaborative filtering. *IEEE Transactions on Image Processing* **16** 2080–2095.

[13] De Lathauwer, L., De Moor, B. and Vandewalle, J. (2000b). On the best rank-1 and rank-$(R_1, R_2, \ldots, R_N)$ approximation of higher-order tensors. *SIAM J. Matrix Anal. Appl.* **21** 1324-1342.

[14] Frank, J. (2006). *Three-dimensional electron microscopy of macromolecular assemblies: visualization of biological molecules in their native state*. Oxford University Press.

[15] Fujisawa, H. and Eguchi, S. (2008). Robust parameter estimation with a small bias against heavy contamination. *Journal of Multivariate Analysis* **99** 2053–2081.

[16] Haselbach, D., Schrader, J., Lambrecht, F., Henneberg, F., Chari, A. and Stark, H. (2017). Long-range allosteric regulation of the human 26S proteasome by 20S proteasome-targeting cancer drugs. *Nature Communications* **8** 15578.

[17] Haselbach, D., Komarov, I., Agafonov, D. E., Hartmuth, K., Graf, B., Dybkov, O., Urlaub, H., Kastner, B., Lührmann, R. and Stark, H. (2018). Structure and conformational dynamics of the human spliceosomal Bact complex. *Cell* **172** 454–464.

[18] Hohn, M., Tang, G., Goodyear, G., Baldwin, P. R., Huang, Z., Penczek, P. A., Yang, C., Glaeser, R. M., Adams, P. D. and Ludtke, S. J. (2007). SPARX, a new environment for Cryo-EM image processing. *Journal of Structural Biology* **157** 47–55.

[19] Hung, H., Huang, S.-Y. and Ing, C.-K. (2020). A generalized information criterion for high-dimensional PCA rank selection. *arXiv:2004.13914*.

[20] Hung, H., Wu, P.-S., Tu, I.-P. and Huang, S.-Y. (2012). On Multilinear Principal Component Analysis of Order-two Tensors. *Biometrika* **99** 569-583.

[21] Katsevich, E., Katsevich, A. and Singer, A. (2015). Covariance matrix estimation for the cryo-EM heterogeneity problem. *SIAM Journal on Imaging Sciences* **8** 126–185.

[22] Konishi, S. and Kitagawa, G. (1996). Generalised information criteria in model selection. *Biometrika* **83** 875–890.

[23] Li, B., Kim, M. K., Altman, N. et al. (2010). On dimension folding of matrix- or array-valued statistical objects. *The Annals of Statistics* **38** 1094–1121.

[24] Maaten, L. v. d. and Hinton, G. (2008). Visualizing data using t-SNE. *Journal of Machine Learning Research* **9** 2579–2605.

[25] Manning, C. D., Raghavan, P. and Schütze, H. (2008). *Introduction to Information Retrieval*. Cambridge University Press.

[26] Mead, A. (1992). Review of the Development of Multidimensional Scaling Methods. *Journal of the Royal Statistical Society. Series D* **41** 27-39.

[27] Pan, V. Y. and Chen, Z. Q. (1999). The complexity of the matrix eigenproblem. In *Proceedings of the thirty-first annual ACM symposium on Theory of Computing* 507–516. ACM.

[28] Penczek, P. A., Kimmel, M. and Spahn, C. M. (2011). Identifying conformational states of macromolecules by eigen-analysis of resampled cryo-EM images. *Structure* **19** 1582–1590.

[29] Punjani, A., Rubinstein, J. L., Fleet, D. J. and Brubaker, M. A. (2017). cryoSPARC: algorithms for rapid unsupervised cryo-EM structure determination. *Nature Methods* **14** 290.

[30] Scheres, S. H. (2012). RELION: implementation of a Bayesian approach to cryo-EM structure determination. *Journal of Structural Biology* **180** 519–530.

[31] Serna, M. (2019). Hands on Methods for High Resolution Cryo-Electron Microscopy Structures of Heterogeneous Macromolecular Complexes. *Front. Mol. Biosci.* **6**.

[32] Shiu, S. Y. and Chen, T. L. (2012). Clustering by self-updating process. eprint arXiv:1201.1979.

[33] Sorzano, C. O. S., Bilbao-Castro, J. R., Shkolnisky, Y., Alcorlo, M., Melero, R., Caffarena-Fernandez, G., Li, M., Xue, G., Marabini, R. and Carazo, J. M. (2010). A clustering approach to multireference alignment of single-particle projections in electron microscopy. *Journal of Structural Biology* **171** 197-206.

[34] Stein, C. M. (1981). Estimation of the mean of a multivariate normal distribution. *Ann. Statist.* **9** 1135–1151.

[35] Tao, D., Sun, J., Wu, X., Li, X., Shen, J., Maybank, S. J. and Faloutsos, C. (2007). Probabilistic tensor analysis with Akaike and Bayesian information criteria. In *International Conference on Neural Information Processing* 791–801. Springer.

[36] Tu, I.-P., Huang, S.-Y. and Hsieh, D.-N. (2019). The Generalized Degree of Freedom of Multilinear Principle Component Analysis. *Journal of Multivariate Analysis* **173** 26–37.

[37] Ulfarsson, M. O. and Solo, V. (2008). Dimension estimation in noisy PCA with SURE and random matrix theory. *IEEE Transactions on Signal Processing* **56** 5804–5816.

[38] Van Heel, M. and Frank, J. (1981). Use of multivariates statistics in analysing the images of biological macromolecules. *Ultramicroscopy* **6** 187–194.

[39] van Heel, M., Portugal, R. V. and Schatz, M. (2016). Multivariate statistical analysis of large datasets: Single particle electron microscopy. *Open Journal of Statistics* **6** 701.

[40] Wong, W., Bai, X.-c., Brown, A., Fernandez, I. S., Hanssen, E., Condron, M., Tan, Y. H., Baum, J. and Scheres, S. H. (2014). Cryo-EM structure of the Plasmodium falciparum 80S ribosome bound to the anti-protozoan drug emetine. *Elife* **3** e03080.

[41] Yang, Z., Fang, J., Chittuluru, J., Asturias, F. J. and Penczek, P. A. (2012). Iterative stable alignment and clustering of 2D transmission electron microscope images. *Structure* **20** 237-247.

[42] Ye, J. (2005). Generalized low rank aapproximation of matrices. *Machine Learning* **61** 167-191.

[43] Zhao, Z., Shkolnisky, Y. and Singer, A. (2016). Fast steerable principal component analysis. *IEEE Transactions on Computational Imaging* **2** 1–12.

[44] Zhao, Z. and Singer, A. (2014). Rotationally invariant image representation for viewing direction classification in cryo-EM. *Journal of Structural Biology* **186** 153–166.

SZU-CHI CHUNG
INSTITUTE OF STATISTICAL SCIENCE
ACADEMIA SINICA
TAPEI, TAIWAN, 11529
E-mail address: phonchi@stat.sinica.edu.tw

SHAO-HSUAN WANG
INSTITUTE OF STATISTICAL SCIENCE
ACADEMIA SINICA
TAPEI, TAIWAN, 11529
E-mail address: pico@stat.sinica.edu.tw

PO-YAO NIU
INSTITUTE OF STATISTICAL SCIENCE
ACADEMIA SINICA
TAPEI, TAIWAN, 11529
E-mail address: po.niu@email.ucr.edu

SU-YUN HUANG
INSTITUTE OF STATISTICAL SCIENCE
ACADEMIA SINICA
TAPEI, TAIWAN, 11529
E-mail address: syhuang@stat.sinica.edu.tw

WEI-HAU CHANG
INSTITUTE OF CHEMISTRY
ACADEMIA SINICA
TAPEI, TAIWAN, 11529
E-mail address: weihau@chem.sinica.edu.tw

I-PING TU
INSTITUTE OF STATISTICAL SCIENCE
ACADEMIA SINICA
TAPEI, TAIWAN, 11529
E-mail address: iping@stat.sinica.edu.tw